Journal of Applied Physics ARTICLE scitation.org/journal/jap

Ion acceleration in a wall-less Hall thruster

Cite as: J. Appl. Phys. **130**, 093302 (2021); doi: 10.1063/5.0062607
Submitted: 6 July 2021 · Accepted: 7 August 2021 ·
Published Online: 2 September 2021

Jacob Simmonds[1,2,a)] and Yevgeny Raitses[2,a)]

AFFILIATIONS

[1]Mechanical and Aerospace Engineering, Princeton University, Princeton, New Jersey 08544, USA
[2]Princeton Plasma Physics Laboratory, Princeton, New Jersey 08543, USA

Note: This paper is part of the Special Topic on Physics of Electric Propulsion.
[a)]**Authors to whom correspondence should be addressed:** jacobbs@princeton.edu and yraitses@pppl.gov

ABSTRACT

In wall-less Hall thrusters, the ionization of the propellant and the acceleration of the ions occur outside the thruster [S. Mazouffre, S. Tsikata, and J. Vaudolon, in *50th AIAA/ASME/SAE/ASEE Joint Propulsion Conference* (American Institute of Aeronautics and Astronautics, Cleveland, OH, 2014)]. This reduces interactions between the plasma and the thruster parts as compared to conventional annular and cylindrical Hall thrusters and promises a longer thruster lifetime. With a much simpler design, these non-conventional thrusters are also easier to miniaturize for operation at low power levels of a few hundred watts and lower. In this work, experiments demonstrate that a miniaturized (3 cm diameter) 200 W wall-less thruster is also able to achieve similar voltage utilization, propellant utilization, and current utilization efficiencies as conventional Hall thrusters. Yet, thruster performance of the wall-less thruster is generally lower due to a much larger plume divergence than that in conventional Hall thrusters. This plume divergence is a consequence of ion acceleration in the fringing magnetic field. Thrust and plasma measurements suggest that the thrust generated by the wall-less thruster is due to two components: ion acceleration by the JxB force in the region of the fringing magnetic field radially away from the thruster and by plasma expansion in the diverging magnetic field near the thruster axis.

I. INTRODUCTION

The ion-induced erosion of Hall thruster channel walls remains one of the key limitations to the development of long lifetime Hall thrusters for deep space missions. While state-of-the art thrusters are capable of achieving lifetimes on the order of 10 000 h,[2,3] this erosion limits the thrust density and size of these thrusters. This issue is particularly relevant to miniaturized low power (<200 W) Hall thrusters: for conventional annular geometry Hall thrusters, the miniaturization leads to higher plasma and heat fluxes to the channel walls. In addition to wall erosion, these losses are also responsible for the typical lower efficiencies of miniaturized Hall thrusters compared to their larger counterparts.[4] Accordingly, there has been recent interest in altering the design of Hall thrusters to limit this erosion, such as shaping the magnetic field to achieve magnetic shielding of the channel walls.[5–10] This has culminated in well-developed miniaturized thrusters, such as MaSMi, which is expected to achieve lifetimes of up to 28 000 h.[11,12] Another approach is to remove the plasma-facing walls and rely on alternate magnetic geometries. This approach was investigated with the cylindrical Hall thruster (CHT), where the inner channel walls of the Hall thruster were removed.[13] The removal of the central magnetic circuit leads to plasma residing in a strong axial magnetic field, which alters the physics of the device compared to conventional annular Hall thruster designs and has led to much research on these thrusters.[4,14–17] Recent studies of a miniaturized CHT revealed a substantial erosion of the backwall in this thruster.[18] It was also suggested that an increase in the magnetic mirror at the back wall could help to mitigate the erosion.[19] Further removal of the outer channel walls leads to the wall-less Hall thruster design, where both ionization and acceleration occur outside the thruster body. This type of Hall thruster was first developed by Kapulkin *et al.*[20] but has seen recent development.[1,21–23] Recent measurements of a 500 W wall-less Hall thruster (WLHT) and the low-power external-discharge plasma thruster (XPT) have shown inefficiencies due to low voltage utilization (low energy of accelerated ions compared to the applied voltage) and large plume divergence. The WLHT, for instance, displays mean ion energies of about 50% of the discharge voltage and a plume angle of 60°,[24] while the XPT has demonstrated a plume angle of 50°.[21,22] This lower efficiency compared to the typical annular Hall thruster (voltage utilization:

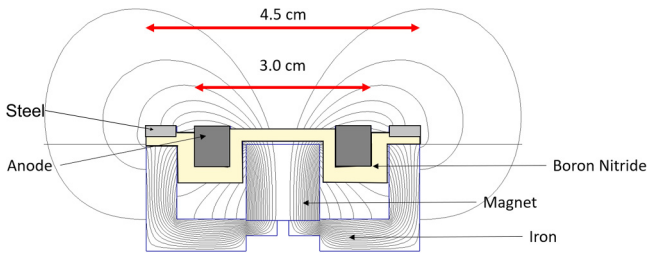

FIG. 1. Magnetic field of the MET thruster simulated with nonlinear finite element method software.[35]

90% and 40° plume angle)[25–28] has quelled interest in wall-less geometry despite potential lifetime advantages.

In this article, we report recent results of plasma and performance studies of a miniaturized 3 cm wall-less Hall thruster (Fig. 1). The thruster magnetic field topology has two distinctive regions: (i) a fringing topology with a strong radial component of the magnetic field in front of the anode and (ii) a diverging axial magnetic field in the vicinity of the thruster axis. In each of these regions, electrons are bouncing along the magnetic field lines between the magnetic mirror at the thruster axis and the plasma-wall sheath at the opposite side of the magnetic field lines [for region (i)] and the cathode potential in the plume [for region (ii)]. Thus, electrons are trapped along the magnetic field lines in a so-called magneto-electrostatic trap (MET). In this article, we refer to this wall-less Hall thruster as the thruster with a magneto-electrostatic trap or an MET thruster. The measured results suggest that in the MET thruster, the ion acceleration in both region (i) and region (ii) contributes to the thrust. The ion acceleration in the fringing magnetic field (region i) is similar to that of conventional Hall thrusters with ExB fields, while the ion acceleration in the diverging magnetic field (region ii) is likely due to plasma expansion in this region. The latter is similar to what was observed and used in end-Hall thrusters or grid-less Kaufman sources.[29–31] This region also exists to an extent in the CHT[4,32] and likely to a smaller extent in miniaturized annular Hall thrusters.[33,34] Interestingly, our measurements suggest comparable contributions to ion acceleration and thrust from both regions.

This article is organized as follows: In Sec. II, we discuss the principle of operation of the MET thruster. The experimental diagnostics and procedures are reviewed in Sec. III. In Sec. IV, we describe our experimental results that are split into following types: (a) measurements of ions in the thruster plume, (b) spatial measurements of the plasma potential and density in the ionization and acceleration regions, (c) performance measurements of the MET thruster, (d) plasma potential measurements in the center of the thruster and a discussion of mechanisms for its formation, and (e) an analysis of the thrust generation in the MET thruster. Our main conclusions are given in Sec. V.

II. DESIGN CONSIDERATIONS OF THE MET THRUSTER

The magnetic field of the MET thruster is generated by a single central Samarium Cobalt (SmCo) permanent magnet placed behind the thruster plasma-facing (PF) wall (Fig. 1). Results of non-linear magnetostatic simulations of the magnetic field in the MET thruster are shown in Fig. 2. The magnet is located in a magnetic core made from a high magnetic permeability low carbon steel, which directs the magnetic flux to produce high radial fields near the thruster anode (Fig. 2), while reducing magnetic leakage out of the thruster body. The thruster plasma-facing (PF) wall is made from a boron nitride (BN) ceramic. The thruster anode is encased in this BN piece and is located near the region of high radial magnetic fields. The laboratory thruster described in this article has a characteristic size (anode diameter) of 3 cm and operates between 200 and 500 W (30–70 W/cm^2) with temperatures below the working temperature of the SmCo magnet (~300 °C). No active cooling is used. In comparison, state-of-the-art annular Hall thrusters typically operate with lower power densities of 25 W/cm^2, while the WLHT[1] and XPT[22,36] have been shown to each operate at ~20 W/cm^2.

A strong magnetic field inhibits the electron flow to the anode as the electrons can only move across field lines either because of their collisions with neutral atoms and ions or through scattering by plasma fluctuations. An estimate of the ionization length

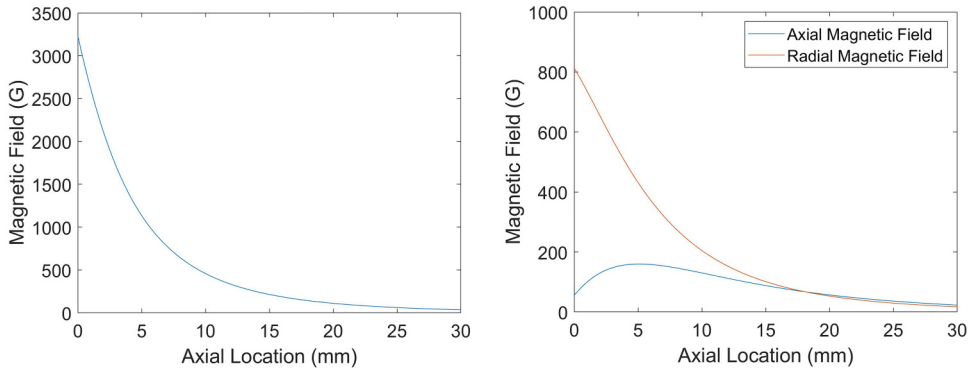

FIG. 2. Axial magnetic field vs axial location in the center of the thruster (left). Axial and radial magnetic field vs axial location above the anode median (R = 1.2 cm) (right).

provides a qualitative view of the direction of ion acceleration. If we take the mean free path of ionization to be $\lambda_i = v_n/(n_e\langle\sigma v_e\rangle)$, where v_n is the neutral velocity (assumed to be thermal with 700 K temperature),[37] n_e is the plasma density that is taken to be 10^{12} cm^{-3} (a typical value of the maximum plasma density in Hall thrusters),[4] σ is the electron-Xenon neutral collision ionization cross section,[38] and v_e is the mean electron velocity, we can calculate the ionization mean free path of xenon atoms. By assuming electron temperature to be a tenth of the applied voltage of 300 V, as has been measured in Hall thrusters,[39] we get the ionization rate to be $\langle\sigma v_e\rangle \sim 1.5 \times 10^{-7}$ cm^{-3}/s and the ionization mean free path is 0.14 cm. This length is well within the region of high radial magnetic fields ≤1 cm (Fig. 2). Thus, the effective ionization of the xenon gas supplied through the anode can be sustained within this region. This result is in agreement with previous predictions for the XPT thruster.[22] Under the assumption of equipotential magnetic field surfaces, it is anticipated that the majority of ions would be borne by the anode in a region of a strong radial magnetic field and, following Ref. 40, a strong axial electric field. The inward-pointing asymmetry of magnetic fields was implemented to facilitate some degree of focusing of the ion plume by the associated inward radial electric fields.

Electrons move along the magnetic field lines and are confined by a magnetic mirror in the thruster center and the thruster edge, where the plasma-wall sheath is likely a dominant repelling mechanism. This effect of electron magnetic mirroring has been described in other wall-less thrusters[22] and demonstrated in particle-in-cell (PIC) simulations.[41] Magnetic mirroring of electrons has also been described in CHTs,[17,42] where electrons instead are repelled by the high gradient in the axial magnetic field in the center and accelerated back toward the thruster body by low plume potentials. We note that as discussed in this article, it is in the center of the MET that we observe a strong electric field in the axial direction, i.e., along the magnetic field lines.

III. EXPERIMENTAL SETUP

A. Facility

Experiments were conducted in a 28 m^3 vacuum vessel equipped with three cryopumps that achieve a base pressure of 10^{-8} Torr, corrected for xenon. This facility is described elsewhere.[13] The xenon gas flow rate was measured with an MKS flow controller with a full scale of 15 SCCM and ±0.1 SCCM uncertainty. The anode flow rate in the thruster was varied in the range of 2–12 SCCM of xenon. A commercial hollow cathode (Fig. 3) was used as a cathode neutralizer and operated with a xenon flow rate of 2 SCCM, a cathode keeper current of 1.2 A, and a keeper voltage of 20 V. During thruster experiments, the background gas pressure in the vacuum vessel did not exceed 2 μTorr, corrected for xenon.

B. Diagnostics

Thrust was measured with a torsion balance thrust stand with two Riverhawk 5032-800 flex pivots to provide the restoring torque. A Micro-Epsilon optoNCDT-1420 laser was used for displacement measurements of the thrust stand. This provided a measurable thrust range of 0–50 mN with measurement uncertainty of ±0.03 mN due to the resolution of the laser.

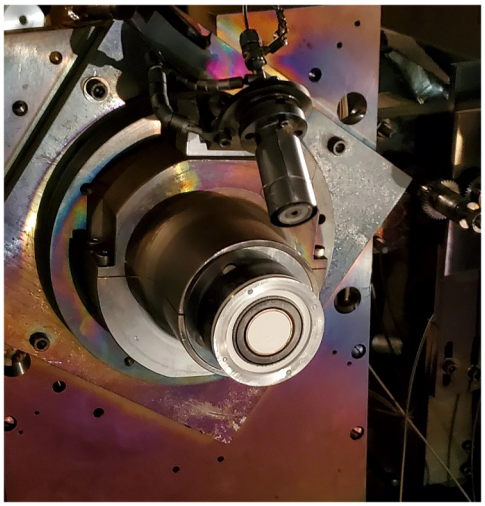

FIG. 3. A 3 cm diameter MET thruster in the vacuum chamber. A hollow cathode-neutralizer is visible above the thruster.

The plume diagnostics used in these experiments, including a planar probe and a retarding potential analyzer (RPA), are described elsewhere.[15,27,43,44] Plume measurements were conducted with a planar probe of diameter 1 cm at a distance of 73 cm from the channel exit that was rotated ±90° relative to the thruster axis. The probe was biased −40 V with respect to ground and has a guarding sleeve to minimize possible edge effects. This bias voltage was sufficient to reach saturation of the ion current collected by the probe. Ion energy was measured with a retarding potential analyzer (RPA) on this same rotating system, which allowed angular measurements of ion energy. The RPA in use was a two-grid system, which operates by applying a positive sweeping voltage to the first grid with respect to ground, which repels ions of energy/charge below this sweeping voltage. A second grid is negatively biased to repel electrons, resulting in the collected current constituting of ions above the sweeping voltage. The ion energy distribution function (IEDF) is found by finding the derivative of the collected current with respect to the sweeping voltage, and the mean ion energy is defined as the mean energy value over this distribution. The ratio of the mean ion energy to the applied anode voltage gives voltage utilization η_{volt}.

For plasma potential measurements, floating emissive probes were used. These probes are composed of 0.025 cm tungsten wire in alumina tubing with segmented graphite ringlet shielding, which have been found to reduce disturbances to the plasma.[45] These probes were placed on a high-speed positioning system to provide spatial measurements. This positioning system has been described elsewhere.[27] The same emissive probes without applied heating (i.e., cold probe) were used for the measurements of ion current distribution to deduce ion density distribution. For these measurements, the probe was connected to the ground and so floated negatively with respect to the plasma along the probe insertion path.

Finally, a separate stationary probe made from a 0.025 cm tungsten wire inserted in alumina tubing was placed near the thruster edge to monitor the effect of probe-induced plasma disturbances on the floating potential.

C. Measurement procedures

1. Thrust and plume

Thrust measurements were made after the steady-state operation of the thruster was achieved, which occurred after 20 min of operation. At this point, the thruster temperature was relatively stable, but a long timescale thermal drift of the equilibrium position of the thrust stand occurred due to heating by the thruster. To minimize these thermal effects, each thrust measurement was determined by measuring the displacement of the thrust stand as the thruster is operating and as it is turned off. The instantaneous equilibrium position at the time of thruster operation could then be determined, and the thrust was calculated by scaling the difference in displacement positions by the measured effective spring constant. This effective spring constant was re-calibrated periodically throughout the experiment with a motor-operated weight–pulley system that applied a known 19 mN force, and the spring constant was found to be almost unaffected by the heat. Each thrust measurement was repeated five times to determine a statistical error, which was found to be ±0.4 mN. We define specific impulse I_{sp} and efficiency η_{anode} in relation to the measured thrust (T), the mass flow rate through the anode ($\dot{m}$), and discharge power through the anode (P),

$$I_{sp} = \frac{T}{\dot{m}}, \tag{1}$$

$$\eta_{anode} = \frac{T^2}{2\dot{m}P}. \tag{2}$$

The total ion current (I_i) obtained by the integration of the measured ion angular distribution was used to estimate ion current utilization, propellant utilization, and plume divergence. The current utilization is a measure of the total ion current generated in the thruster vs the discharge current in the power supply (I_d): $\cdot\ \eta_{current} = I_i/I_d$. The propellant utilization is the ratio of the mass flow of ionized propellant vs the input propellant ($\dot{m}$): $\cdot\ \eta_{prop} = MI_i/(e\,\dot{m})$. The plume divergence is a measure of the amount of ions accelerated in the radial direction, which does not contribute to thrust. In Hall thruster literature, this is typically defined in one of two ways: the 90% plume half-angle or the momentum-weighted angle. The 90% plume half-angle is commonly used to measure the extent of plume divergence, which corresponds to the off-axis angle at which 90% of the ion current is measured,

$$0.90\left(2\pi r_p^2 \int_0^{\pi/2} j_i \sin\theta\, d\theta\right) = 2\pi r_p^2 \int_0^{\theta_{90\%}} j_i \sin\theta\, d\theta, \tag{3}$$

where r_p is the distance between the probe face and the thruster, j_i is the measured ion current, θ is the off-axis probe angle, and $\theta_{90\%}$ is the 90% plume half-angle. In contrast, the momentum-weighted angle is related to the plume divergence efficiency as it relates the average angle at which ions are accelerated, assuming constant ion velocity over the plume angle. This angle θ_{mom} is written as

$$\theta_{mom} = \cos^{-1}\left(\frac{\pi r_p^2 \int_{-\pi}^{\pi} j_i \sin\theta\cos\theta\, d\theta}{\pi r_p^2 \int_{-\pi}^{\pi} j_i \sin\theta\, d\theta}\right). \tag{4}$$

The momentum-weighted angle relates to thruster efficiency η_{total} by plume divergence efficiency η_{div}, assuming there is no angle dependence of ion velocity,

$$\eta_{div} = \cos^2\theta_{mom}, \tag{5}$$

$$\eta_{total} = \eta_{div}\eta_{current}\eta_{prop}\eta_{volt}. \tag{6}$$

2. Plasma properties

The plasma potential ϕ and electron temperature T_e were determined by measuring the floating potential of both emissive and cold probes (ϕ_e and ϕ_c, respectively) and relating their relative sheath potentials under the assumption of the Maxwellian electron energy distribution function (EEDF):[46] $\phi = \phi_e + 1.5T_e$ and $T_e = \frac{(\phi_e - \phi_c)}{4.27}$.[4] This factor of 1.5 is consistent with the measurements of the sheath at emitting surfaces in flowing plasmas such as those that exist in Hall thrusters.[47]

Plasma density measurements were conducted in the thick sheath regime, as the approximate measured sheath thickness (~0.1 cm) was over two times larger than the probe diameter. Plasma density was determined by relating the collected ion saturation current to plasma density for the expanding sheath:[48] $n = \frac{I_i\pi}{2eA_p}\sqrt{-\frac{2M}{eV}}$, where A_p is the probe area, V is the probe potential with respect to the surrounding plasma, and e is the charge of the electron. Here, we also assumed the EEDF to be Maxwellian and assumed ions were singly charged.

Throughout all measurements of spatial properties reported in this article, both the discharge current and a stationary floating probe near the thruster edge monitored plasma disturbances induced by fast probe insertion. In the reported measurements, the disturbances of the discharge current and the floating potential of the stationary probe did not exceed 10% of their steady-state values. Representative plots of probe-induced disturbances of these parameters are shown in Appendix A.

Note that due to harsh plasma environments near the thruster PF wall, the emissive probes only survived 1–3 insertions each experiment, and so plasma potential and electron temperature were only collected at one operating regime of the MET thruster: 250 V discharge voltage and 6 SCCM flow rate. Plasma potential and electron temperature were measured along the anode median and 0.3 cm radial increments above the median. Measuring at radial positions below the anode median resulted in the emissive probe immediately burning up, and so spatial measurements were not obtained there.

IV. RESULTS AND DISCUSSION

A. Plume measurements

The angular ion current distribution in the plume of the MET thruster was measured for xenon gas flow rates between 2 and

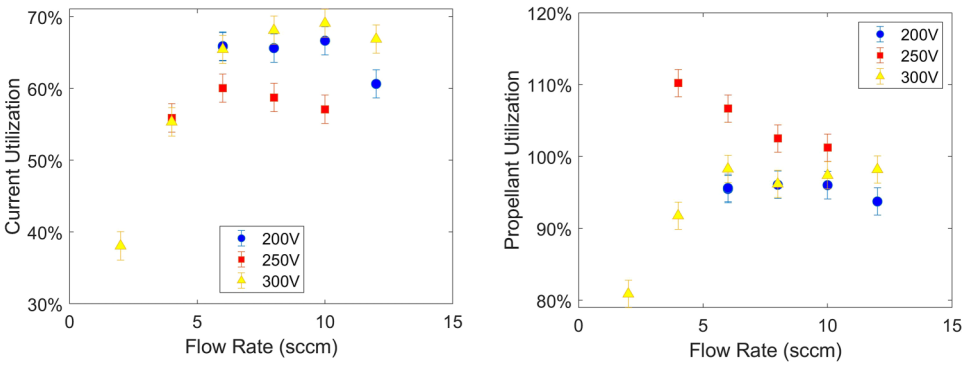

FIG. 4. Effect of the xenon gas flow rate on propellant utilization (left) and current utilization (right) for different discharge voltages. Error bars in both plots correspond to one standard deviation of multiple measurements taken at the regime with the flow rate of 6 SCCM and the discharge voltage of 300 V.

12 SCCM and discharge voltages of 200, 250, and 300 V (Fig. 5). Measurements of propellant utilization (Fig. 4) show that 90%–100% of propellant is ionized at discharge voltages of 200 and 300 V, with a slight increase as the flow rate increases. Curiously, at discharge voltages of 250 V, the propellant utilization exceeded unity. This result is similar to that observed for the CHTs at similar voltages.[14] In Ref. 14, measurements of state-of-charge of ions in CHTs showed that such unusually high propellant utilization is due to a large fraction of multiply charged ions present in the plume of the CHT. It is reasonable to suggest that multi-charged ions are also generated by the MET thruster, which can explain the propellant utilization of higher than unity measured at the discharge voltage of 250 V. As the ionization mean free path is inversely proportional to the plasma density, the increase in propellant utilization is expected with the gas flow rate. The current utilization (Fig. 4) of the MET thruster ranges between 60% and 70%, which is a significant source of inefficiency in the MET thruster. This high electron current will be analyzed in Sec. II.

The plume angle deduced from the measured angular ion current distribution (Fig. 5) for the MET thruster is shown in Fig. 6. The plume tends to become more focused as the mass flow increases. This can be particularly seen for discharge voltages of 300 V. These results are generally similar to that of other wall-less thrusters.[21,22,24] The momentum-weighted angle [Eq. (4)] ranges between 36° and 45° for the MET thruster, while the 90% plume angle [Eq. (3)] ranges between 62° and 72°. As it is shown in Sec. IV B of this article, this large plume divergence is likely due to ionization and ion acceleration in the fringing magnetic field where the electric field is defocusing.

Figure 7 shows the IEDF measured at different angular positions of the RPA with respect to the thruster [Fig. 7(a)] and the angular distribution of the mean ion energy [Fig. 7(b)]. The IEDF has a relatively large population of low energy ions [Fig. 7(a)], which may imply an overlap between ionization and acceleration regions or some contribution from charge-exchange collisions. Measurements of mean ion energy show an overall efficient acceleration of ions with energies of 85%–90% of the applied voltage, both on-axis and 90° off-axis (Fig. 7). A curious feature of the results shown in Fig. 7(b) is the presence of the minimum mean ion energy between 30° and 60°: the mean ion energy was higher at 90° off-axis than angles closer to the axis. This high mean ion energy with the minimum at ~45° off-axis occurred over all measurements. Physical mechanisms responsible for this behavior are not understood at the moment and require further studies. The high mean energies of ions at large plume angles are also unusual: in conventional Hall thrusters, ion energy decreases at large angles.[49] For the MET thruster, this waste of power into radial acceleration is apparently a source of inefficiency.

B. Plasma properties in ionization and acceleration regions

The measured distribution of the plasma potential is shown in Fig. 8 with magnetic field lines superimposed. Interestingly, the equipotential assumption appears to only weakly hold near the anode. The acceleration region near the anode median is also shown to be within 0.6 cm of the thruster PF wall, with an expanded potential structure by the anode edge. Such a "spike" of potential was also observed in other Hall thrusters and attributed

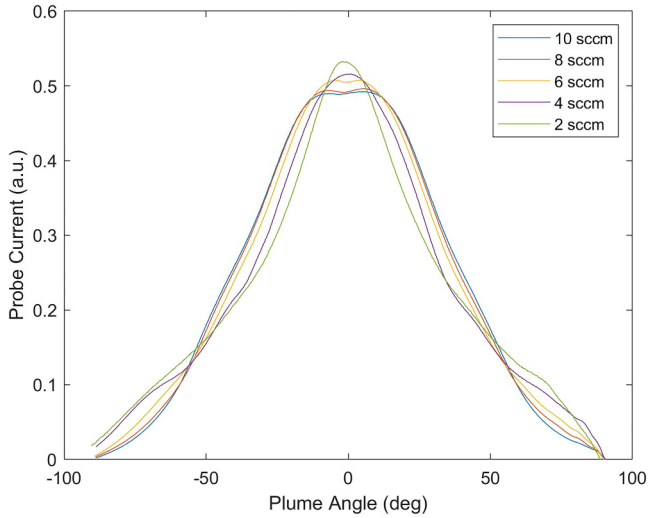

FIG. 5. Measured angular ion current distribution for the MET thruster at 300 V between 2 and 10 SCCM. Ion current distribution is normalized by the total ion current.

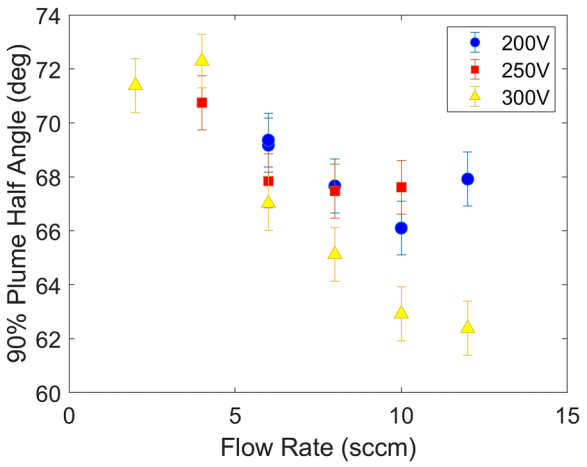

FIG. 6. Plume narrowing with the increase in the xenon gas flow. Measurement uncertainties are estimated to be ±1° for the plume angle.[14]

to electron fluxes along the magnetic field lines that alter the magnetic field surfaces from equipotentiality.[50] For conventional annular Hall thrusters, it was theorized that these radial fluxes are caused by radial pressure gradients along the magnetic field lines and differences between magnetic field topology at the inner and outer walls of the annular thruster channel. In the MET thruster, a strong magnetic field and pressure gradients in the radial direction exist as well. They may also account for a significant departure of equipotentials from magnetic field surfaces. The resulting radial electric fields may be responsible for large plume divergence and high energy of ions accelerating from the thruster at large plume angles. There also exists considerable inward-focusing electric fields, which suggest that ions are being focused toward the center of the thruster. These ions are either accelerated past the center to contribute to divergence losses or experienced some outward force to "straighten" the ions toward the axis, as has been suggested in CHTs.[51]

Similar to all Hall thrusters, the electron cross-field current ($I_e = I_d - I_i$) in the MET thruster is much larger than the electron current expected to be carried out by classical collisional processes. This can be shown using a one-dimensional Ohm law,

$$I_e = \left(en_e\mu(E + \frac{1}{en}\nabla_z P\right)A_{anode}, \tag{7}$$

where A_{anode} is the anode area, $\frac{1}{en}\nabla_z P$ is the plasma pressure gradient toward the thruster exit (approximately −20 V/cm, from plasma density and electron temperature measurements), E is the electric field (~200 V/cm, from the plasma potential measurements), and μ is the electron cross-field mobility. Here, the electron cross-field mobility is

$$\mu = \frac{e}{m_e}\frac{\nu}{\nu^2 + e^2B^2/m_e^2}, \tag{8}$$

where m_e is the electron mass and ν is the electron collision frequency. Using measured spatial variations of the plasma properties (plasma potential and the plasma density) and the magnetic field at the anode median, we can estimate the collision frequency that is required to match the measured current utilization [Fig. 4(b)].[40] For the MET thruster, this collision frequency is on the order of 10^9 Hz that is three orders of magnitude higher than that expected by electron–neutral collisions. Note that this anomalously high collision frequency is of the same order as that of the Bohm value $\nu_B \sim \frac{eB}{16\,m_e} \sim 10^9$Hz.[40] Thus, the enhanced electron cross-field current explains the relatively low current utilization observed in the MET and reported in Sec. III of this article, as compared to propellant and voltage utilization. This enhanced transport can be attributed to the presence of strong plasma oscillations such as the ExB rotating spoke, which has been shown to increase the electron cross-field transport.[52] Indeed, the azimuthal spoke oscillations were also observed and measured in the MET thruster and the WLHT.[41,53] Results of these measurements in the MET thruster will be reported in a separate article.

Measurements of the plasma potential (Fig. 8) and plasma density (Fig. 9) show the acceleration region to be within 1 cm of the anode and the ionization region to be within ~0.3 cm from the thruster anode. This ionization region appears to be small due to high electron temperatures in the region, as the measured electron energy reached ~20 eV within 1 cm of the anode (Fig. 10). The high electron temperatures may account for high propellant utilization determined from plume measurements (Fig. 4). The measured

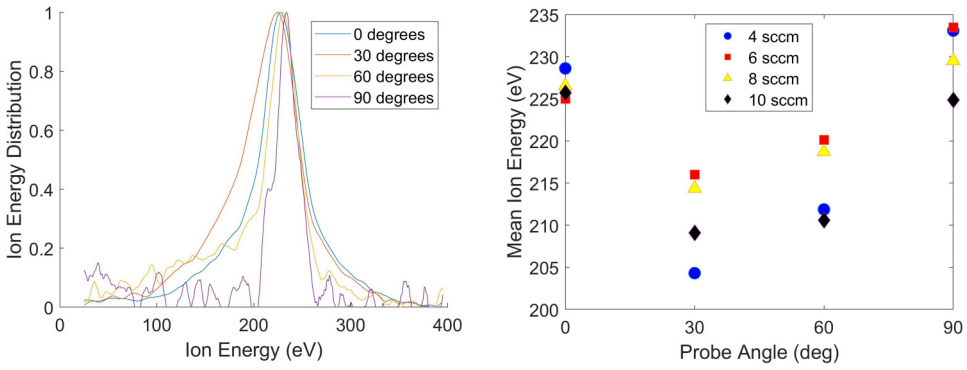

FIG. 7. Results of the measurements of the ion energy distribution function (IEDF) of the MET thruster operating at 250 V: (a) IEDF at several plume angles with y axis normalized for comparison over an angle measured at 6 SCCM (left) and (b) the effect of the xenon gas flow rate on the angular distribution of the mean ion energy (right). The full width at half-maximum of the IEDF is ~40 eV.

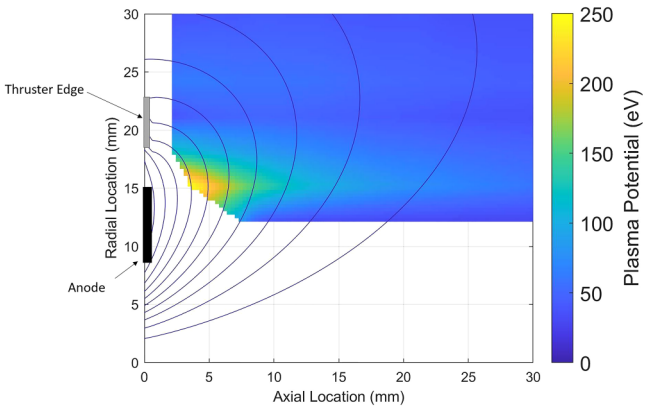

FIG. 8. Plasma potential profile measured in the MET thruster operating at the discharge voltage of 250 V and a xenon gas flow rate of 6 SCCM. The magnetic field lines obtained from non-linear magnetostatic simulations are superimposed. Region of probe disturbance removed from the plot (see Appendix A).

data do appear to fit both the prediction of electron temperatures that are ~1/10 of the applied voltage[39] and the associated short ionization length. Furthermore, there is another peak of plasma density at the center of the thruster. Here, the plasma density is comparable to the maximum plasma density measured near the anode (Fig. 9). Measurements at the thruster center (Fig. 11) show temperatures as high as 40 eV, which correspond to ionization mean free paths of ~0.1 cm.

From plasma potential measurements along the thruster centerline, the potential profile appears to be similar to that observed in the near anode region with a strong radial magnetic field (Fig. 11). Here, a plasma potential of 230 V was measured 1 cm from the thruster. The presence of a such a high plasma potential in the central region of the MET is not understood at the moment,

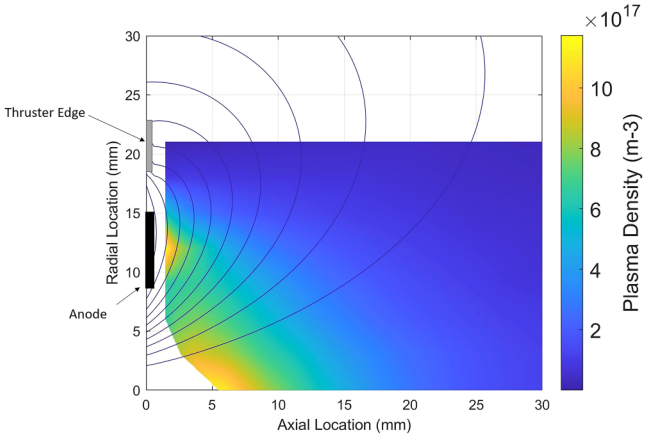

FIG. 9. Density profile measured in the MET thruster operating at the discharge voltage of 250 V and a xenon gas flow rate of 6 SCCM. The magnetic field lines obtained from non-linear magnetostatic simulations are superimposed. Region of probe disturbance removed from the plot (see the Appendix A).

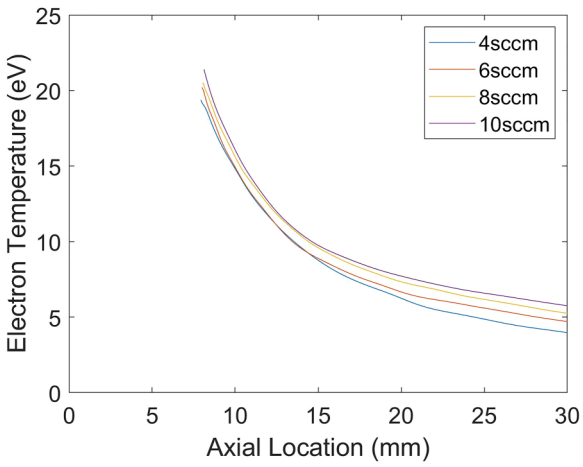

FIG. 10. Effect of the gas flow rate on the electron temperature distribution along the axis of the MET thruster at 1.5 cm from the thruster centerline (the outer edge of the anode). Measurements were conducted for the discharge voltage of 250 V.

but it may be associated with a high ambipolar potential due to high electron temperatures [~40 eV; Fig. 11(b)] or some enhancement of electron cross-field transport between the near-anode region and the thruster center, causing the plasma near the thruster surface to be about the anode potential. A somewhat similar result was also measured in the CHT, though the presence of a short annular channel caused the measured potential to be almost 2.5 times lower than the anode voltage (250 V).[4] However, unlike for the CHT case, measurements for the MET thruster show a strong potential drop along the centerline toward the plume [Fig. 11(a)]. At a distance between 1.5 and 2 cm from the thruster, the plasma potential drops from 200 to 100 V.

In principle, under the assumption of equipotential magnetic field surfaces, one would expect the magnetic field lines at the thruster axis of both the MET thruster and the CHT to be closer to the cathode potential. Apparently, this is not what was observed in the experiments for both thrusters. Moreover, LIF measurements in CHT showed ion acceleration along the thruster axis.[54] It was suggested that this acceleration is due to the effects of supersonic rotation of the electrons in the Hall thruster plasma—it has been shown that the centrifugal force of the electrons deflects the electric field axially, straightening the force vector and pushing a component of the electric field along the magnetic field line.[51] The extent to which this is responsible for the potential along central field lines needs further investigation. Other potential explanations include pressure gradients leading to a rapid plasma expansion in the diverging magnetic field, or perhaps the presence of a strong magnetic mirror may be responsible for strong variations of the electric potential along the magnetic field lines.[55] However, the magnetic mirror effect would require anisotropy of the EEDF, which to our knowledge has only been simulated[56,57] and never measured for the wall-less thrusters and for Hall thrusters in general.

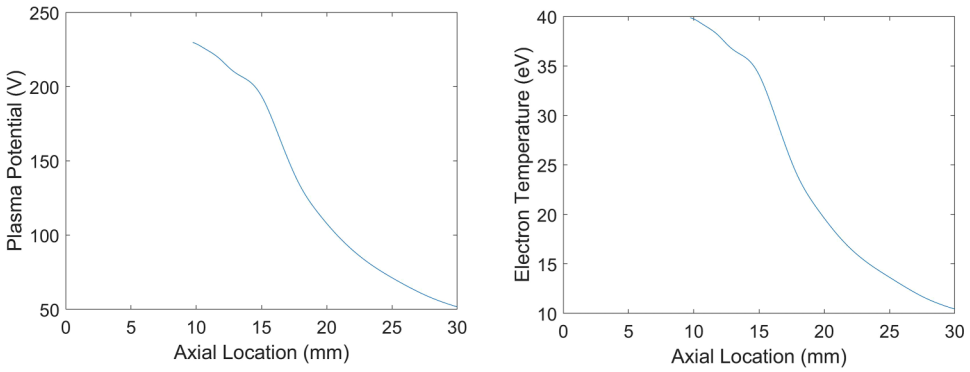

FIG. 11. Spatial profiles of the plasma potential (left) and the electron temperature (right) measured in the center of the MET thruster at the discharge voltage of 250 V and the xenon flow rate of 6 SCCM. Results are only shown for the region with minimal probe-induced plasma disturbances. These disturbances are discussed in Appendix A (see Fig. 16).

The presence of strong pressure gradients along the magnetic field lines with peak plasma density at the thruster center is confirmed by results of the probe measurements of plasma density (Fig. 9). The peak density at the center of the thruster has a similar magnitude to the maximum plasma density in the vicinity of the anode. A similar radial density profiles with a characteristic peak at the thruster center were also observed in the miniaturized 2.6 cm CHT thruster. It was proposed that this density peak is a result of the electrostatic trapping of low energy ions produced by charge-exchange collisions in this region of the thruster with counter-streaming ion flows accelerated from the anode region of the CHT.[32,58]

From plasma potential and plasma density measurements near the MET thruster, it appears that this thruster has two regions from which ions are accelerated and generate the thrust by two distinctive mechanisms. For the near anode region of the MET thruster, the ion acceleration is likely dominated by ExB fields due to the high radial magnetic fields, while for the thruster center, the ions are accelerated by an electric field along the magnetic field lines. This electric field is likely formed by a combined operation of ambipolar effects due to the pressure gradients along the diverging magnetic field and magnetic mirror effects.

Interestingly, for the CHT, the maximum plasma potential and the maximum plasma density at the axis and the plasma appear to be affected by the thruster diameter. For example, for a 9 cm diameter CHT thruster, the potential was about 40 V, which is about twice smaller than that of the smaller 2.6 cm diameter counterpart.[4] Note that the xenon flow rate of the 9 cm CHT was only three times larger than the flow rate of the 2.6 cm CHT, leading to an increase in the neutral density of roughly a magnitude of four. In contrast to the 2.6 cm CHT, the MET thruster operates with a higher mass flow and consequently has a neutral density roughly double that of the 2.6 cm CHT as well as higher plasma potential and density in the center. The scaling of the plasma potential and plasma density at the thruster center for these smaller thrusters may imply that the ion acceleration in a diverging magnetic field may be characteristic of miniaturized thrusters with applied magnetic fields (i.e., Hall thrusters, CHTs, wall-less Hall thrusters, etc.). This result may be somewhat general as the divergence of the magnetic field in the center increases as the thruster diameter decreases, whether by design or through simple scaling of the thruster size, and this increase in magnetic divergence may lead to higher ion acceleration driven by mirror or ambipolar pressure effects. The position of the anode may also have some effect on this central potential profile, as measurements have shown the general discharge characteristics and the efficiency of the miniaturized CHT is heavily dependent on this position.[59]

C. Performance measurements

Thrust and power increased somewhat linearly with the flow rate (Fig. 12). A small increase in specific impulse with the flow rate is also observed. This increase in specific impulse appears to be driven by the decrease in plume divergence with the flow rate (Fig. 6), as mean ion energy was relatively constant with the flow rate (Fig. 7). The higher specific impulse resulted in an increase in efficiency from ~14% to ~20% when the flow rate increased from 6 to 12 SCCM. A relatively low efficiency of this thruster appears to be primarily due to large plume divergence and, to a lesser extent, low current utilization. Plume divergence efficiency as defined by Eq. (5) gave values of ~50%, which is much lower than conventional Hall thrusters, while current utilization was ~60%–70% (Fig. 6). This is in contrast to high propellant utilization (>90%) and voltage utilization (~90%) in Figs. 4 and 7, respectively. Measurements of off-axis ion energy (Fig. 7) may explain some of this inefficiency; ions at large plume angles were measured with high energies that do not contribute to thrust. In contrast, Hall thrusters typically have low ion energy at large plume angles, i.e., less power wasted on ions accelerated radially to large plume angles.[49]

D. Remarks on the magnetic mirror effect

The mechanism of the ion acceleration in the central part of the MET thruster requires more detailed theoretical and experimental studies. In this regard, one of the most interesting results reported here is a strong potential difference along the magnetic field lines at the thruster centerline. While the high potential (~230 V) can be described by the formation of a sheath along the floating thruster surface, the physics behind the strong electric field is currently unknown, as the measured plasma pressure gradient is lower than the electric field, implying some other mechanism than ambipolar plasma expansion is at play (Fig. 13). This mechanism could be due to a variety of factors, such as electron centrifugal effects on the electric field,[51] magnetic nozzle effects, or magnetic mirror effects. In this section, we shall consider the possible effect

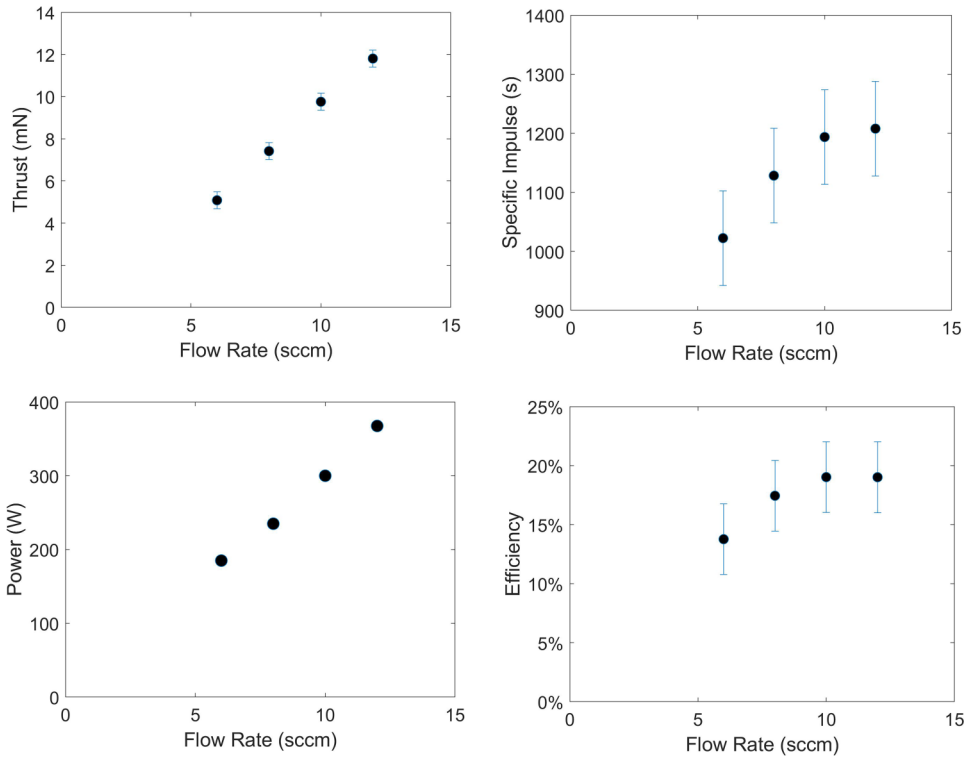

FIG. 12. Measured performance of the MET thruster operated at the discharge voltage of 250 V: Thrust (top-left), specific impulse (top-right), power (bottom-left), and efficiency (bottom-right).

of the magnetic mirror on the potential difference in this region, such as that found in the diverging section of a typical magnetic nozzle.[60] The plasma acceleration in the diverging magnetic field or magnetic mirror with an applied electric field was previously considered for propulsion application by Kaufman *et al.*, where it was determined that this magnetic mirror generated an ion-accelerating electric field in the end-Hall thruster for non-magnetized ions.[30] They measured a roughly similar potential drop (~70–100 V) along the axial magnetic field. This potential drop was approximated by the following relation:

$$V_1 - V_2 = kT_e/e \ln\left(\frac{B_1}{B_2}\right), \tag{9}$$

where V_1 and V_2 are the plasma potentials upstream and downstream, respectively, and B_1 and B_2 are the magnetic field upstream and downstream, respectively. The end-Hall thruster geometry is similar to the central region of the MET thruster. Extending Kaufman's analysis, the electron fluid momentum balance equations in the center of the thruster relate the electric field to magnetic mirror pressure and the plasma pressure by taking into account the anisotropy of the electron energy,[61]

$$E_z \sim \frac{1}{e}\left(\frac{T_\parallel - T_\perp}{B}\right)\frac{dB}{dz} - \frac{1}{en}\frac{d(nT_\parallel)}{dz}, \tag{10}$$

where $T_\parallel$ is the electron energy along the magnetic field, $T_\perp$ is the energy orthogonal to the magnetic field, and B is the magnetic

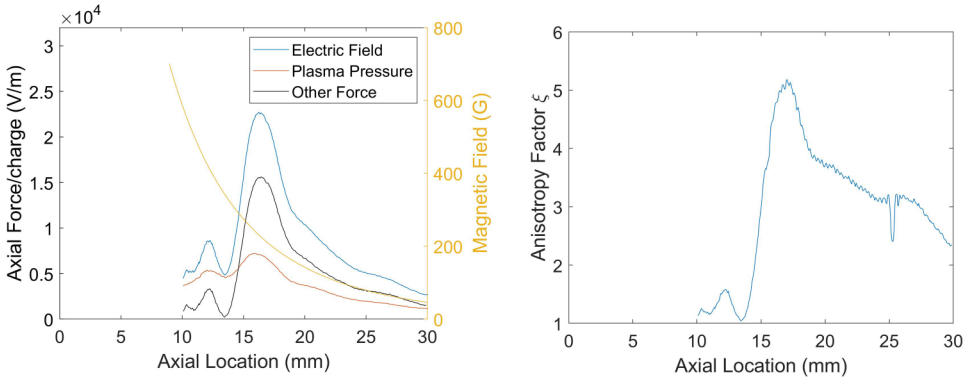

FIG. 13. Analysis of the magnetic mirror effect in the MET thruster: (a) Measured axial electric field, plasma pressure, and the unaccounted force vs axial location in the thruster center (left). Magnetic field in the center is shown for reference and (b) estimated electron energy anisotropy factor vs axial location (right). Here, $\xi = 1$ constitutes a fully isotropic plasma, assuming unaccounted force is due to magnetic mirroring.

field. Here, we have neglected plasma resistivity in the center as this term is much smaller than the electric field in the worst-case scenario where all current (1 A) flows through the central region of radius 0.4 cm (plasma resistivity ~0.01 V/cm and E ~ 200 V/cm). Although there is no experimental evidence of electron temperature anisotropy for Hall thrusters including for conventional annular Hall thrusters, CHT and wall-less thrusters, PIC simulations have predicted anisotropic EEDF with electron energy in the direction of perpendicular to the magnetic field (i.e., in the direction of the electric field) to be several times higher than that parallel to the magnetic field.[56] The heating of electrons by the electric field and losses of energetic electrons to walls were the main causes of this anisotropy in simulations. Another source of the anisotropy could be the injection of electrons from the cathode to the diverging magnetic field. Energetic electrons from the cathode may result from the acceleration of the thermionically emitted electrons in the cathode sheath or generated in the hollow cathode plasma. It is not clear whether any of these mechanisms can be applied for our analysis of the MET thruster, but it is instructive to determine what level of anisotropy is required to explain the potential difference along the field line measured in the wall-less thruster. For that purpose, we introduce the factor of anisotropy ξ that is determined by equating the measured electric field and the plasma pressure to the unaccounted force (Fig. 13), which is assumed to be the magnetic mirror force. Here, $\xi = 1$ represents a fully isotropic plasma,

$$T_\perp = \xi\, T_\parallel, \tag{11}$$

$$E_z = -\frac{1}{en}\left(\frac{(\xi-1)nT_\parallel}{B}\frac{dB}{dz} + \frac{d(nT_\parallel)}{dz}\right), \tag{12}$$

$$\xi = \frac{B}{nT_\parallel \dfrac{dB}{dz}}\left(-E_z en - \frac{d(nT_\parallel)}{dz}\right) + 1. \tag{13}$$

The emissive probe diagnostic used in this study did not solely measure the parallel portion of electron temperature as the probe is larger than the electron gyroradius, and so the measurements of electric field, density, and electron temperature cannot be used in Eq. (13) to definitively determine this anisotropic factor. Future work to measure the anisotropy of the electron energy in this region would be instrumental in determining the contribution of the magnetic mirror to the electric field in this region. In the absence of such measurements, under the assumption that the temperature measured in the emissive probe was in the parallel direction, we could come up with some estimate of the anisotropy factor using Eq. (13). Plots of this estimate are shown in Fig. 13, where the deduced anisotropy of the electron energies is relatively isotropic in the plume ($\xi \sim 1$ at >3 cm from the thruster surface) and is anisotropic in the acceleration region where the gyromotion electron energy appears to dominate by a factor of 5. While this appears to follow what would be expected in a magnetic mirror, it should be stressed that this is under dubious assumption that the emissive probe is measuring the parallel electron temperature.

We note that under the above assumptions, the electrons should become isotropic upstream of the high electric field about 1 cm from the thruster. Calculations of the relative frequencies in the plasma show that the electron gyrofrequency (~10^{10} Hz) is several orders of magnitude above the electron neutral collision frequency (~10^6 Hz) and the electron–electron collision frequency (~10^7 Hz) (see the Appendix B), and so it is unlikely that isotropization is the result of electron collisions with other particles. Physical mechanisms that may potentially be responsible for this isotropization include, but are not limited to, plasma instabilities such as the spoke or the interaction of plasma electrons trapped in the MET thruster and secondary electrons emitted from the boron nitride wall. For electron temperatures above 30 eV, the secondary electron emission from the boron nitride can reach 100%.[62] The role of plasma instabilities and the plasma–material interaction in forming this central acceleration region, both in magnitude and in position, requires further investigation. We note that if this isotropization is maintained near the thruster surface and the mirror is nullified, we would expect a sheath to form on the thruster surface with the following corresponding plasma potential: $\Delta V_{floating} \approx T_e\left(0.5 + \ln\sqrt{\frac{M}{2\pi m_e}}\right) = 230\ V$. This may explain the high plasma potential observed in the thruster center; however, measurements of electron energy anisotropy are required to verify this.

Swirl acceleration in magnetic nozzle thrusters can form a significant portion of the thrust.[60] This thrust is generated when magnetized ions are demagnetized and, due to the conservation of energy, transfer their azimuthal energy to axial energy. This is generally not found in Hall thrusters as the magnetic fields are chosen such that only electrons are magnetized. However, in the center of the MET thruster, xenon ions with thermal velocities, such as those newly ionized by electron–neutral collisions or charge exchange, are magnetized due to their low gyroradius of ~0.1 cm, which is well below the length scale of the thruster. The high plasma density in the center of the thruster (Fig. 9) suggests there may be a considerable population of magnetized xenon ions. However, it is unlikely that swirl acceleration plays a large role in the xenon-fed MET thruster, as the ions cannot gain more than ~1 eV of energy in gyromotion before losing magnetization. Still, the relatively strong axial component of the applied magnetic field (Fig. 2) may affect the trajectory of new ions and warrants further investigation.

E. Remarks on contributions of different regions to thrust

The presence of peak plasma density at the center of the thruster and a strong electric field along the magnetic field may constitute a significant portion of the thrust. The degree to which this contributes to the total thrust can be calculated with the plasma potential and density measurements. The thrust in each area of interest was calculated as

$$T = \int_{R_0}^{R_f} 2\pi r \int neE_z\, dz\ \ dr, \tag{14}$$

where R_f and R_0 are the upper and lower radial bounds of the integrating area. For the sake of this simplified analysis, the center portion of the thruster is considered to be within 0.4 cm radius (where the density is high in Fig. 9) and assumes that the plasma potential profile in this region is the same as that measured along

the centerline. The anode portion is considered to be between 0.9 and 1.5 cm radius. Through this method, the total thrust calculated for this 6 SCCM regime was 4.8 mN, which is in agreement with the measured thrust of 5 mN (Fig. 12). The fraction of thrust due to acceleration from the near anode region is then found to be ~80%, while the fraction in the center is ~20%. This suggests that an appreciable portion of the thrust is due to non-Hall acceleration and underlies the nonconventional behavior of the MET thruster. This result may also be applicable to similar miniaturized plasma thrusters with ExB fields. Curiously, the corresponding thrust densities in both regions are comparable, ~8.5 N/m^2.

Note that in the above analysis of thrust generation, we neglected ion acceleration by the plasma pressure gradient toward the back wall of the MET thruster. In principle, if this acceleration takes place, the generated thrust should be compensated by the ion dynamic pressure on the backwall. Although the net thrust by ions would be zero, this would cause erosion of the back wall. This effect depends on the potential drop between the plasma and the back wall. Future studies of plasma–wall interaction in the MET will explore if this effect is relevant to the MET.

V. CONCLUSIONS

The MET thruster demonstrates high propellant (90%–100%) and voltage utilization (~90%), implying that efficient operation of wall-less thruster types may be possible with further development. This high propellant utilization is due to a short ionization region (<0.5 cm) formed near the thruster surface, which appears to occur because of high electron temperatures (~20–40 eV) measured in this region. In this respect, the MET thruster is similar to other wall-less thrusters, such as XPT. Despite these advantages, plume divergence and current utilization remain a concern, as each lowers the total efficiency by ~50% and ~60%, respectively. The current utilization is likely driven by plasma instabilities such as the spoke, however some methods have demonstrated the capability to suppress this spoke instability through the addition of segmented anodes with resistive circuitry[52] or externally driving the breathing mode by modulating the anode voltage.[63] The acceleration of ions to high energies at large off-axis plume angles is also a large source of thruster inefficiency that needs to be addressed in future designs. This large plume divergence is of particular practical concern for operation on spacecraft: the plume may impinge on spacecraft components such as solar panels, and so it is critical to focus the plume further. Were this plume divergence to be reduced such that all ions were accelerated axially, the efficiency of this thruster would be comparable to that of a conventional Hall thruster at low powers: ~35%–40% at 200 W.[12]

Measurements of plasma potential demonstrated an acceleration region within 1 cm of the thruster anode in a region of high magnetic field. While the ion acceleration in the near-anode region is driven by an electric field setup by impeding the electron flow in the axial direction across the magnetic field, the axial electric field of a similar magnitude (~200 V/cm) was measured in the center of the thruster where the magnetic field is axial, and electrons can move axially bouncing along the field lines between the magnetic mirror near the thruster and the cathode potential in the plume. Plasma potentials close to the applied voltage were measured in the central region and dropped along the field lines toward the cathode. The mechanism behind this central acceleration region is still unclear. For example, the plasma pressure gradient is too small to account for this electric field. It is suggested that the magnetic mirroring of the electrons in the center could play a significant role in this acceleration. Measurements found a high plasma density both near the anode (away from the thruster centerline) and in the center of the thruster. This suggests that both the center of the thruster and a peripheral region of the thruster around the anode play comparable roles in thrust generation. One of the implications of this result is that unlike annular Hall thrusters with coaxial channels in which plasma is bounded by inner and outer walls, the MET thruster utilizes the whole thruster area to generate the thrust.

ACKNOWLEDGMENTS

This work was supported by the U.S. Department of Energy under Contract No. DE-AC02-09CH11466. The authors would like to thank Andrei Smolyakov, Igor Kaganovich, and Nirbhav Chopra for fruitful discussions. The authors also thank Timothy Bennett, Peter Sloboda, Steve Jurczynski, and Tucker Hill for technical assistance.

APPENDIX A: PROBE PERTURBATIONS

Insertion of probes into the thruster plasma, particularly when the probe is emitting electrons, leads to significant disturbances of the Hall thruster plasma. Data shown in this article are limited to where probe disturbances were minimal—within ~10% of the

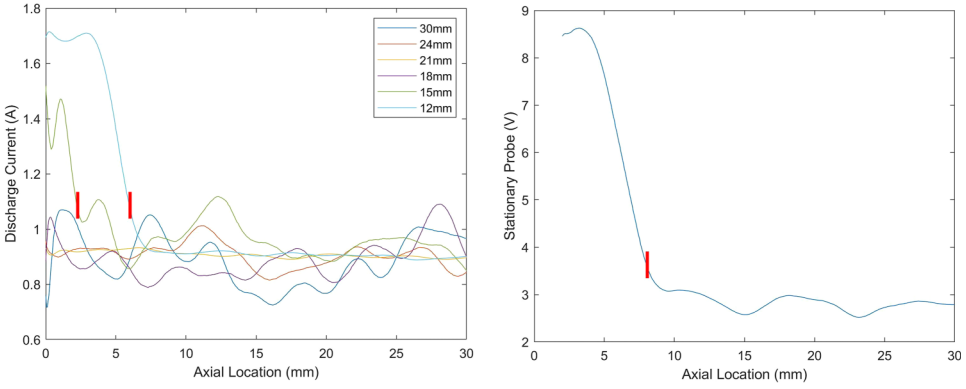

FIG. 14. Measured plasma disturbance during insertion of the emissive probe at multiple radial positions as measured by discharge current (left) and stationary probe signal (right) for 1.2 cm radial position. Data shown in Fig. 8 are to the right of the red lines.

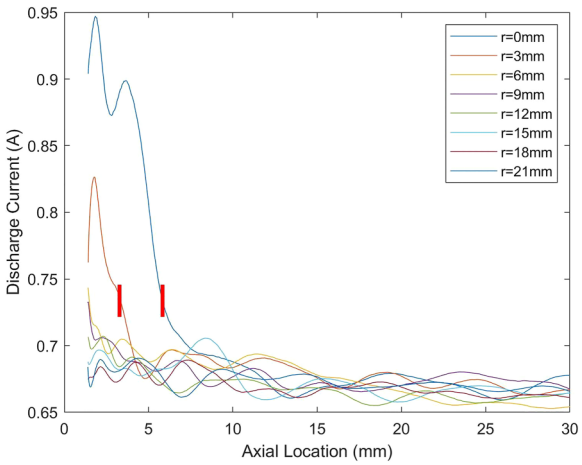

FIG. 15. Measured plasma disturbance during insertion of the cold probe at multiple radial positions as measured by the discharge current. Data shown in Fig. 9 are to the right of the red lines for radial positions 0 and 3 mm.

nominal value. Figure 14 shows measured probe disturbance from the hot emissive probe at multiple radial positions as observed in the discharge current, and the stationary probe at 1.2 cm radial position. Figure 15 shows measured probe disturbance from the cold density probe at multiple radial positions. Only discharge current data were used in this regime to determine probe disturbance, as stationary probe data were unavailable. Figure 16 shows measured probe disturbance from the hot emissive probe in the center of the thruster, which shows disturbances at a higher axial location than near the anode, likely due to the high plasma density measured there (Fig. 9).

APPENDIX B: COLLISION FREQUENCY ESTIMATES

Estimates of the electron–electron and electron–neutral collision frequency were made assuming the following conditions: magnetic field $B = 1000$ G, xenon atoms, electron temperature $T_e = 40$ eV, plasma density $n_e = 10^{18}\,\mathrm{m}^{-3}$, neutral density $n_n = 10\ n_e$, electron–neutral momentum rate coefficient $k_m = 2.5 \times 10^{-13}\,\mathrm{m}^3/\mathrm{s}$, and the Coulomb logarithm $\ln \Lambda_e = 16$. The electron–neutral collision collision frequency was found to be $\nu_{en} = n_n k_m = 2.5\,\mathrm{MHz}$, and the electron–electron collision frequency was $\nu_{ee} = \frac{n_e e^4}{\sqrt{m_e T_e^3 \epsilon_0^2}} \ln \Lambda_e = 8.7$ MHz.

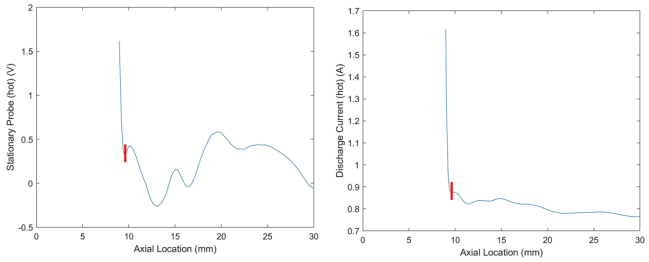

FIG. 16. Measured plasma disturbance during insertion of the emissive probe in the center of the thruster as measured by (left) discharge current and (right) the stationary probe signal. Data shown in Fig. 11 are to the right of the red line.

DATA AVAILABILITY

The data that support the findings of this study are available within the article.

REFERENCES

[1]S. Mazouffre, S. Tsikata, and J. Vaudolon, in *50th AIAA/ASME/SAE/ASEE Joint Propulsion Conference* (American Institute of Aeronautics and Astronautics, Cleveland, OH, 2014).
[2]B. A. Arhipov, A. S. Bober, R. Y. Gnizdor, K. N. Kozubsky, A. I. Korakin, N. A. Maslennikov, and S. Y. Pridannikov, in *Proceedings of the International Electric Propulsion Conference 1995* (Electric Rocket Propulsion Society, Moscow, 1995).
[3]N. A. Maslennikov, in *Proceedings of the International Electric Propulsion Conference 1995* (Electric Rocket Propulsion Society, Moscow, 1995).
[4]A. Smirnov, Y. Raitses, and N. J. Fisch, J. Appl. Phys. **95**, 2283 (2004).
[5]I. G. Mikellides, I. Katz, R. R. Hofer, and D. M. Goebel, Appl. Phys. Lett. **102**, 023509 (2013).
[6]I. Mikellides, I. Katz, R. Hofer, and D. Goebel, in *48th AIAA/ASME/SAE/ASEE Joint Propulsion Conference & Exhibit* (American Institute of Aeronautics and Astronautics, Atlanta, GA, 2012).
[7]L. Grimaud, J. Vaudolon, S. Mazouffre, and C. Boniface, in *52nd AIAA/SAE/ASEE Joint Propulsion Conference* (American Institute of Aeronautics and Astronautics, Salt Lake City, UT, 2016).
[8]I. Levchenko, K. Bazaka, Y. Ding, Y. Raitses, S. Mazouffre, T. Henning, P. J. Klar, S. Shinohara, J. Schein, L. Garrigues, M. Kim, D. Lev, F. Taccogna, R. W. Boswell, C. Charles, H. Koizumi, Y. Shen, C. Scharlemann, M. Keidar, and S. Xu, Appl. Phys. Rev. **5**, 011104 (2018).
[9]T. Andreussi, V. Giannetti, A. Leporini, M. M. Saravia, and M. Andrenucci, Plasma Phys. Control Fusion **60**, 014015 (2018).
[10]L. Grimaud and S. Mazouffre, Plasma Sources Sci. Technol. **26**, 055020 (2017).
[11]R. Lobbia, R. W. Conversano, A. Lopez Ortega, S. Reilly, and I. G. Mikellides, in *36th International Electric Propulsion Conference* (University of Vienna, Austria, 2019).
[12]R. W. Conversano, D. M. Goebel, R. R. Hofer, I. G. Mikellides, and R. E. Wirz, J. Propul. Power **33**, 975 (2017).
[13]Y. Raitses and N. J. Fisch, Phys. Plasmas **8**, 2579 (2001).
[14]K. D. Diamant, J. E. Pollard, Y. Raitses, and N. J. Fisch, IEEE Trans. Plasma Sci. **38**, 1052 (2010).
[15]Y. Raitses, E. Merino, and N. J. Fisch, J. Appl. Phys. **108**, 093307 (2010).
[16]A. Shirasaki and H. Tahara, J. Appl. Phys. **101**, 073307 (2007).
[17]Y. Jiang, H. Tang, J. Ren, M. Li, and J. Cao, J. Phys. D: Appl. Phys. **51**, 035201 (2018).
[18]W. Mao, H. Sun, Y. Ding, W. Xu, Y. Hu, H. Li, L. Wei, and D. Yu, Vacuum **162**, 145 (2019).
[19]Y. Hu, W. Xu, W. Mao, and Y. Ding, Jpn. J. Appl. Phys. **59**, 046002 (2020).
[20]A. M. Kapulkin, A. D. Grishkevich, and V. F. Prisnyakov, in *Proceedings of the 45th IAF Congress, Space Technology* (Jerusalem, Israel, 1995), pp. 391–394.
[21]B. Karadag, Ph.D. thesis (The Graduate University for Advanced Studies (SOKENDAI), 2018).
[22]B. Karadag, S. Cho, and I. Funaki, J. Appl. Phys. **123**, 153302 (2018).
[23]J. Simmonds and Y. Raitses, in *The 36th International Electric Propulsion Conference* (University of Vienna, Austria, 2019).
[24]S. Mazouffre, S. Tsikata, and J. Vaudolon, J. Appl. Phys. **116**, 243302 (2014).

[25]R. R. Hofer, R. S. Jankovsky, and A. D. Gallimore, J. Propul. Power **22**, 721 (2006).
[26]J. McVey, E. Britt, S. Engelman, F. Gulczinski, E. Beiting, J. Pollard, and R. Cohen, in *39th AIAA/ASME/SAE/ASEE Joint Propulsion Conference and Exhibit* (American Institute of Aeronautics and Astronautics, Huntsville, AL, 2003).
[27]Y. Raitses, D. Staack, A. Dunaevsky, L. Dorf, and N. J. Fisch, *Preliminary Results of Plasma Flow Measurements in a 2 KW Segmented Hall Thruster* (Princeton Plasma Physics Lab., NJ, 2003), p. PPPL-3796.
[28]Y. Raitses, D. Staack, A. Dunaevsky, and N. J. Fisch, J. Appl. Phys. **99**, 036103 (2006).
[29]H. R. Kaufman, R. S. Robinson, and R. I. Seddon, J. Vac. Sci. Technol. A **5**, 2081 (1987).
[30]H. R. Kaufman, R. S. Robinson, M. L. Day, and T. W. Haag, in *21st International Electric Propulsion Conference* (American Institute of Aeronautics and Astronautics, Orlando, FL, 1990).
[31]A. A. Goncharov, I. V. Litovko, A. N. Dobrovolsky, L. V. Najko, and I. V. Najko, Rev. Sci. Instrum. **87**, 02A501 (2016).
[32]A. Smirnov, Y. Raitses, and N. Fisch, in *40th AIAA/ASME/SAE/ASEE Joint Propulsion Conference and Exhibit* (American Institute of Aeronautics and Astronautics, Fort Lauderdale, FL, 2004).
[33]V. Khayms and M. Martinez-Sanchez, in *32nd Joint Propulsion Conference and Exhibit* (American Institute of Aeronautics and Astronautics, Lake Buena Vista, FL, 1996).
[34]A. Smirnov, Y. Raitses, and N. J. Fisch, J. Appl. Phys. **92**, 5673 (2002).
[35]P. Karban, F. Mach, P. Kůs, D. Pánek, and I. Doležel, Computing **95**, 381 (2013).
[36]B. Karadag, S. Cho, I. Funaki, Y. Hamada, and K. Komurasaki, J. Propul. Power **34**, 1094 (2018).
[37]L. Dorf, Y. Raitses, and N. J. Fisch, J. Appl. Phys. **97**, 103309 (2005).
[38]D. Rapp and P. Englander-Golden, J. Chem. Phys. **43**, 1464 (1965).
[39]D. Staack, Y. Raitses, and N. J. Fisch, Appl. Phys. Lett. **84**, 3028 (2004).
[40]J.-P. Boeuf, J. Appl. Phys. **121**, 011101 (2017).
[41]K. Matyash, R. Schneider, S. Mazouffre, S. Tsikata, and L. Grimaud, Plasma Sources Sci. Technol. **28**, 044002 (2019).
[42]A. N. Smirnov, Y. Raitses, and N. J. Fisch, IEEE Trans. Plasma Sci. **34**, 132 (2006).
[43]M. E. Griswold, Y. Raitses, and N. J. Fisch, Plasma Sources Sci. Technol. **23**, 044005 (2014).
[44]Y. Raitses, A. Smirnov, and N. J. Fisch, Appl. Phys. Lett. **90**, 221502 (2007).
[45]D. Staack, Y. Raitses, and N. J. Fisch, Rev. Sci. Instrum. **75**, 393 (2004).
[46]J. P. Sheehan, Y. Raitses, N. Hershkowitz, and M. McDonald, J. Propul. Power **33**, 614 (2017).
[47]B. F. Kraus and Y. Raitses, Phys. Plasmas **25**, 030701 (2018).
[48]Y. Raitses, D. Staack, A. Smirnov, and N. J. Fisch, Phys. Plasmas **12**, 073507 (2005).
[49]J. Ekholm, W. Hargus, C. Larson, M. Nakles, G. Reed, and C. Niemela, in *42nd AIAA/ASME/SAE/ASEE Joint Propulsion Conference & Exhibit* (American Institute of Aeronautics and Astronautics, Sacramento, CA, 2006).
[50]M. Keidar, A. D. Gallimore, Y. Raitses, and I. D. Boyd, Appl. Phys. Lett. **85**, 2481 (2004).
[51]N. Fisch, Y. Raitses, and A. Fruchtman, Plasma Phys. Control. Fusion **53**, 124038 (2011).
[52]C. L. Ellison, Y. Raitses, and N. J. Fisch, Phys. Plasmas **19**, 013503 (2012).
[53]S. Mazouffre, L. Grimaud, S. Tsikata, K. Matyash, and R. Schneider, Plasma Sources Sci. Technol. **28**, 054002 (2019).
[54]R. Spektor, K. D. Diamant, E. J. Beiting, Y. Raitses, and N. J. Fisch, Phys. Plasmas **17**, 093502 (2010).
[55]I. A. Biloiu, E. E. Scime, and C. Biloiu, Appl. Phys. Lett. **92**, 191502 (2008).
[56]I. D. Kaganovich, Y. Raitses, D. Sydorenko, and A. Smolyakov, Phys. Plasmas **14**, 057104 (2007).
[57]D. Sydorenko, A. Smolyakov, I. Kaganovich, and Y. Raitses, Phys. Plasmas **13**, 014501 (2006).
[58]A. Smirnov, Y. Raitses, and N. J. Fisch, Phys. Plasmas **11**, 4922 (2004).
[59]Y. Gao, H. Liu, P. Hu, H. Huang, and D. Yu, Phys. Plasmas **24**, 063518 (2017).
[60]E. Ahedo and M. Merino, Phys. Plasmas **17**, 073501 (2010).
[61]R. H. Comfort, in *Geophysical Monograph Series*, edited by T. E. Moore, J. H. Waite, T. W. Moorehead, and W. B. Hanson (American Geophysical Union, Washington, DC, 1988), pp. 51–53.
[62]A. Dunaevsky, Y. Raitses, and N. J. Fisch, Phys. Plasmas **10**, 2574 (2003).
[63]I. Romadanov, Y. Raitses, and A. Smolyakov, Plasma Phys. Rep. **45**, 134 (2019).